Chemical Geology 265 (2009) 160–170

Contents lists available at ScienceDirect

Chemical Geology

journal homepage: www.elsevier.com/locate/chemgeo

Changes in reactive surface area during limestone dissolution: An experimental and modelling study

Catherine Noiriel [a,*], Linda Luquot [b], Benoît Madé [c], Louis Raimbault [c], Philippe Gouze [b], Jan van der Lee [c]

[a] Laboratoire Géosystèmes, Université de Lille I, CNRS, 59655 Villeneuve d'Ascq, France
[b] Laboratoire Géosciences, Université de Montpellier II, CNRS, 34095 Montpellier, France
[c] Centre de Géosciences, École des Mines de Paris, UMPC, EPHE, CNRS, 77305 Fontainebleau, France

ARTICLE INFO

Article history:
Received 30 January 2008
Received in revised form 29 January 2009
Accepted 30 January 2009

Editor: J. Fein

Keywords:
Reactive surface area
Reactive transport
Modelling
Carbon dioxide
Dissolution
Limestone

ABSTRACT

This study explores the dynamics of porosity and reactive surface area changes during porous limestone dissolution by CO_2-rich water. The Sr and Ca concentrations in both the rock and the outlet solution are used to evaluate the reactive surface area changes of the two rock-forming calcites, i.e. micrite grains and sparite crystals, which have different trace element signatures. The geometric surface area measured with X-ray microtomography decreases slightly whereas the reactive surface area increases continuously with increasing porosity from 20.3 to 30.2%. Surprisingly, changes in reactive surface areas are very different between the two calcites. The reactive surface area changes in the micrite are parabolic while the reactive surface area of sparite increases greatly. The numerical model HYTEC is used to model the change in reactive surface areas during the experiment. Different geometrical models are tested. The model based on spherical-grain dissolution and spherical-pore growth fails to reproduce the experimental results, while the sugar-lump model provides reasonable agreement with the experiment.

1. Introduction

Chemical reactions are common in geological reservoirs and thus may induce mineral dissolution (or precipitation). Porosity increase associated with mineral dissolution is an important process in a range of geological settings and industrial applications including diagenesis, karst formation, well stimulation and carbon dioxide sequestration (e.g. Holloway, 1997; Kaufmann and Braun, 1999; Bachu and Adams, 2003). Long-term sequestration of carbon dioxide (CO_2) in geological formations is a current challenge, given the complexity and range of coupled thermal, hydrological, mechanical, and chemical processes involved. Among others, massive injections of CO_2 into reservoirs may alter the geochemical equilibrium between rock-forming minerals and formation waters. Changes in the solid phase volume lead to rock structure modifications, affecting both flow and transport properties of the porous media. Understanding the interplay between chemical reactions, rock geometry changes and fluid transport properties is critical to achieve better predictions of the CO_2 fate in reservoir rocks.

Chemical interactions between minerals and water are driven by chemical disequilibria that persist in the system. Dissolution occurs when fluids are undersaturated with respect to some minerals, i.e. the ionic activity product is lower than the equilibrium constant. During CO_2 injection into host reservoirs, changes in chemical conditions can occur locally due to CO_2 dissolution in the brine present in the reservoir. Coupled with other changes (e.g. temperature and fluid pressure), an increase in CO_2 partial pressure (P_{CO2}) favours particularly the dissolution of carbonate minerals (e.g. Stumm and Morgan, 2004). Thus, massive injection of CO_2 into a carbonate host reservoir can induce strong dissolution of the matrix and porosity increase.

Porosity changes can be calculated from the volumetric amount of dissolved minerals, which is closely related to mass balance. However, the description of macroscopic dissolution patterns is very complex, since they are influenced by several factors including rock heterogeneities, chemical reaction kinetics and mass transfer (e.g. Steefel and Lasaga, 1990; Jamtveit and Yardley, 1997; Lichtner et al., 1997). In some cases the porosity increase is uniform whereas in other cases, it is localised. As a consequence, flow and transport properties can be dramatically different. A number of experimental and theoretical studies have analysed the influence of dissolution processes on the physical and chemical properties of porous media (e.g. Schechter and Gidley, 1969; Fogler and Rege, 1987; Hoefner and Fogler, 1998; Noiriel et al., 2004). For instance, leading mechanisms, such as pore coalescence (Schechter and Gidley, 1969) and formation of highly

* Corresponding author. Present address: Université de Lille I, UMR Géosystèmes, bât. SN5, av. Paul Langevin, 59655 Villeneuve d'Ascq cedex, France. Tel.: +33 3 20 33 60 14; fax: +33 3 20 43 49 10.
E-mail address: catherine.noiriel@univ-lille1.fr (C. Noiriel).

0009-2541/$ – see front matter © 2009 Elsevier B.V. All rights reserved.
doi:10.1016/j.chemgeo.2009.01.032

conductive flow channels (Daccord et al., 1993; Renard et al., 1998; Golfier et al., 2002) involve particularly complex feedback effects.

Among the parameters that measure how important is the interaction between chemistry and flow, the Damköhler number ($Da = k_d L^*/u$, where k_d is a first-order rate constant [s^{-1}], L^* is a characteristics length [m] and u is the fluid velocity [m s^{-1}]), accounts for the relative contribution of advective transport and chemical reaction in the mass transfer process. At high Da (far from equilibrium), dissolution tends to be dominated by wormhole formation. In contrast, at low Da (for example, when the fluid comes to equilibrium), the dissolution becomes more uniform (Golfier et al., 2002).

While great progress has been made in the understanding of the coupling of chemical reaction kinetics and chemical mass transfer, many fundamental problems remain to be solved before long-term predictions can be envisaged. In particular, reactive transport models may fail to reproduce laboratory experiments or field observations when chemical and flow gradients are strong or porous medium is heterogeneous (Glassley et al., 2002; Meile and Tuncay, 2006). Most reactive transport models follow a macroscopic approach, using equivalent properties averaged at the scale of a representative elementary volume (REV). This allows to solve the mass and energy balance of the chemical system for a homogeneous mixture of liquid, solid phases, aqueous species and, possibly, gases. The pore structure geometry and the spatial arrangement of the different rock-forming minerals are often represented in an abstract manner and the numerical models conceived at the macroscopic scale fail to describe the spatial arrangement of the minerals and pores. Thus, the influence of geometry is most likely underestimated in reactive transport modelling. Improvements in non-invasive 3D imagery allow predictions of macroscopic flow properties from microscopic image data (Bernard, 2005; Fredrich et al., 2006), but modelling of pore-scale reactive transport processes and upscaling them to a macroscopic scale are not yet common practice, despite some recent new developments (Li et al., 2007; Li et al., 2008; Flukiger and Bernard, 2009-this issue). Pore-scale models are essential to bridge the gap between pore-scale observations and feedback mechanisms occurring in the macroscopic environment. However, microscopic information is available, and some pore-scale processes can be taken into account in an integrated manner at the REV scale, i.e. the relationship between porosity, permeability and the liquid-exposed surface area of the matrix-forming minerals.

The aim of this study is to understand the dissolution of a porous limestone which involves a significant change in the reactive surface area as well as in the hydrodynamic properties of the medium including porosity and permeability. All these properties are closely linked to the coupled chemistry-transport processes and the modelling therefore requires a fully coupled approach. Experimental work was carried out to provide datasets, according to a methodology combining chemical analyses of the fluid, chemical characterisation of the solid rock, continuous measurements of the permeability and periodic characterisation of the sample geometry by non-invasive X-ray microtomography. Measurements of major and minor elements both in the solid rock and the outlet solution are used to quantify reactive surface area changes for the two rock-forming calcites, i.e. sparite crystals and micrite grains. The reactive transport code HYTEC was used to model the experiment, and different models for reactive surface area evolution were examined.

1.1. Surface areas of rocks

The reactive surface area is an important parameter, because the mineral–fluid interface partially controls the kinetic behaviour in many geological systems. Thus, the characterization of reactive surface area changes resulting from dissolution or precipitation is a prerequisite to accurate modelling of reactive transport in porous media. Let us consider the dissolution of calcite, for which it is generally admitted that the equation describing the dissolution rate is (Lasaga and Kirkpatrick, 1981):

$$r = S_r \times k_c \times (1 - \Omega_{cal}) \quad (1)$$

with r the calcite dissolution rate (mol s^{-1}), S_r the reactive surface area of the mineral (m^2), k_c the overall kinetic dissolution rate (mol m^{-2} s^{-1}) and Ω_{cal} the calcite saturation index. It is worth noting that, in numerical simulations, the surface area often refers to a specific surface area, i.e. one that is normalized to a volume of water (m^2 m^{-3}). Far from equilibrium and in the absence of inhibiting species, k_c can be described following Plummer et al. (1978):

$$k_c = k_1 a_{H+} + k_2 a_{CO_2} + k_3 \quad (2)$$

with a_i the activity of the species i, k_1, k_2 and k_3 the kinetic rate constants equal to 5.12×10^{-1}, 3.45×10^{-4} and 1.19×10^{-6} mol m^{-2} s^{-1}, respectively at 25 °C. Far from equilibrium and at low pH, the dissolution rate depends essentially on the pH and the reactive surface area.

In the absence of mass transfer changes (i.e., the mass transfer is in steady-state), a change of the dissolution rate is possible due to the variation of the reactive surface area, as chemical reactions proceed. The problem is that the reactive surface area on minerals is generally not directly measurable. Moreover, as dissolution occurs at selected sites on the minerals, the reactive surface area may be smaller than the geometrical surface area (Helgeson et al., 1984). That is why this parameter is often used as a fitting parameter in reactive transport codes (Brosse et al., 2004). Nevertheless, the reactive surface area can be estimated from phenomenological or empirical laws, even if the choice of an adequate surface model is still a matter of debate (Gautier et al., 2001; Lüttge et al., 2003). Most of the models are based on total surface area measurements linked to gas adsorption (Brunauer et al., 1938) or to geometrical constructions (Canals and Meunier, 1995; Le Gallo et al., 1998; Colon et al., 2004). Measurements of the surface area by vertical scanning interferometry, atomic force microscopy, laser confocal microscopy or X-ray tomography are sometimes proposed (e.g. Fredrich et al., 1993; Shiraki et al., 2000; Lüttge et al., 2003; Noiriel et al., 2004). However, the applicability of the experimental values in reactive transport models is limited, since the geometrical surface area strongly depends on the scale at which the process is observed. Nevertheless, expressions based on geometrical constructions remain the most practical to compute surface area changes in geological systems by modelling.

A number of different models based on geometrical constructions have been proposed to relate changes in mineral concentration (or porosity) to changes in reactive surface area (Lichtner, 1988; Emmanuel and Berkowitz, 2005). The simplest representation of a porous medium is a package of spherical grains. If it can be assumed that the porous medium is composed of floating spherical grains, the reactive surface area can be expressed by:

$$S_r = S_{r0}\left(\frac{C}{C_0}\right)^{2/3} \quad (3)$$

where C is the mineral concentration, C_0 the initial mineral concentration and S_{r0} the initial surface area. This model assumes a homogeneous decrease of the grain size with dissolution. Alternatively, it can be assumed that the porous medium is represented by floating spherical pores. Thus, an increase of the reactive surface area with dissolution is expected, according to the following law:

$$S_r = S_{r0}\left(\frac{C}{C_0}\right)^{-2/3} \quad (4)$$

A porous medium can also be represented as a cluster of particles, which dissociate as dissolution progresses, exactly as a sugar lump in a

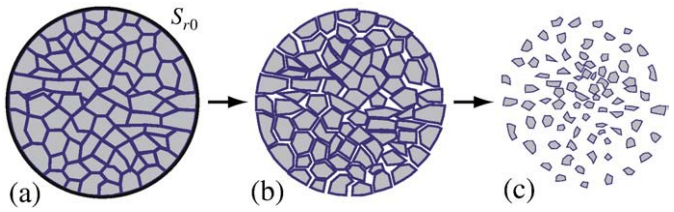

Fig. 1. Dissolution process according to the sugar-lump model. The matrix is composed of (a) spherical grains of surface area S_{r0} (b) which dissociate into smaller grains, thus increasing the water-exposed surface area. (c) Subsequently, the individual particles dissolve which reduces the surface area.

cup of coffee. This process is presented in Fig. 1, showing three steps: (a) the initial, aggregated medium of surface area S_{r0}, (b) dissociation of the particles causing a significant increase of the surface area, (c) dissolution of the individual particles whose surface area decreases with time. According to this model, the reactive surface area can be expressed by:

$$S_r = \left(S_{r0} + S_{rm}\left(1-\left(\frac{C}{C_0}\right)^{n_1}\right)^{n_2}\right)\left(\frac{C}{C_0}\right)^{n_3} \quad (5)$$

where S_{rm} is the maximum surface area given by the sum of the surface areas of all individual particles, n_1, n_2 and n_3 are empiric coefficients that depend on the geometry of the aggregate. For spherical grains, coefficient n_3 is equal to 2/3.

More complex models have also been proposed in the literature. However, the equations presented above already show the possible diversity among representations of reactive surface areas which can evolve in opposite ways. Although some authors have compared the results of experiments made with different models (Colon et al., 2004), the number of experimental studies remains small. Therefore, an effort should be made to identify the behaviour of reactive surface areas in natural systems and evaluate their impact on reactive transport.

2. Materials and methods

2.1. Rock sample

The rock is an Upper Miocene limestone, which was sampled in a borehole drilled in the Campos Basin in Mallorca (Balearic Islands, Spain). It is a pelsparite composed of round micritic peloids separated by secondary microsparitic cement (Fig. 2). Visual observation of sparse ochre spots in the rock may suggest the presence of oxides. The mineralogical composition of the sample was determined by X-ray diffraction (XRD). Only calcite was detected, but two different calcite morphologies were observed within the rock. Micrite is a microcrystalline calcite essentially composed of peloids and micritized fossiliferous material. Sparite is a granular palissadic and blocky calcite cement that probably formed through recrystallization of micrite mud and filling of primary interparticle pores. The proportions of micrite and sparite were estimated on a thin section to be around 60% and 40%, respectively. The porosity is a moldic secondary porosity that was formed by selective leaching of peloids, suggesting a porosity inversion process during diagenesis. Triple-weight porosity measurements give the rock a total porosity ϕ of 15.8%, a connected porosity ϕ_c of 8.9%, and a non-connected porosity ϕ_{nc} of 6.9%.

2.2. Flow-through experiment

The fluid-flow apparatus is shown in Fig. 3. A cylindrical sample, 9 mm in diameter and 15 mm in length was prepared for the flow-through experiment. The core was silicon-coated and jacketed with a Teflon® membrane to seal its periphery. Then the sample was placed in the flow-through cell and saturated with water under vacuum. Note that for the image acquisition (see Section 2.3), the sample was removed from the flow-through cell, but remained saturated. The flow through-cell was then filled with deionised water to avoid the trapping of air bubbles at the inlet of the sample, and the air bubbles trapped at the top of the cell were expelled from the circuit by a rapid flush of fluid.

The experiment was conducted at room temperature (about 20 °C) during 15 h. The inlet fluid used in the experiment was a 0.010 ± 0.001 mol.l^{-1} NaCl solution prepared from reagent-grade NaCl diluted in deionised water. The fluid, initially degassed, was maintained during the experiment at equilibrium with CO_2 at a partial pressure of 0.10 ± 0.01 MPa using a back-pressure regulator. The sample was subjected to the acidic fluid flow at a controlled flow rate of 100 cm^3 h^{-1} (2.78×10^{-8} m^3.s^{-1}) by a dual-piston pump.

During the experiment, the confining pressure was maintained at the same fluid pressure at the sample inlet. The pressure at the inlet was measured with a Keller® sensor in the range of $0–0.3 \pm 0.00015$ MPa. At the outlet, the pressure was kept constant at about 0.13 MPa by a back-pressure regulator to avoid CO_2 degassing in the

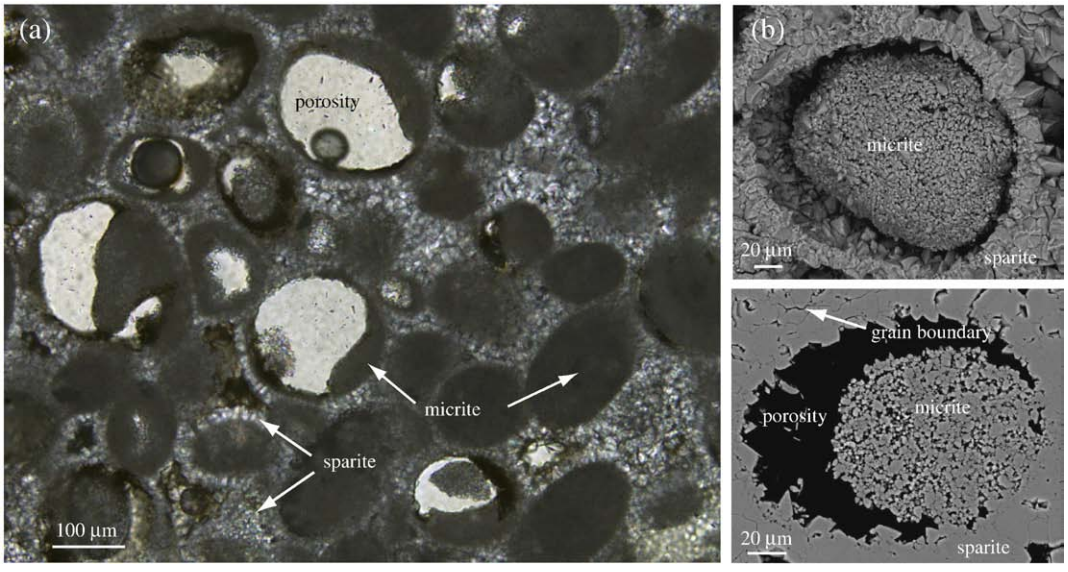

Fig. 2. (a) Thin section of the rock observed with optical microscopy in transmitted light. (b) Scanning electron microscopy (SEM) observations of the sparite and the micrite.

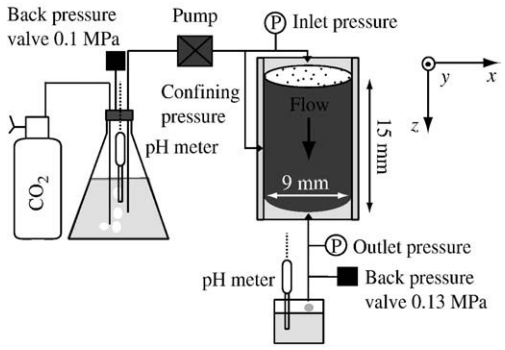

Fig. 3. Schematic representation of the flow-through experimental setup.

circuit. At the inlet, the pH in the fluid was recorded continuously to detect potential CO_2 saturation changes ($pH = 3.9 \pm 0.1$). The different parameters were recorded continuously by a Keithley KPCI-3116 acquisition card monitored with a Labview® program.

Permeability measurements were conducted by measuring the pressure difference ΔP between the sample inlet and outlet. According to Darcy's law, ΔP is directly related to the permeability of the sample, k, by:

$$k = -\mu \times L \times Q / (S \times \Delta P) \quad (6)$$

where L is the length of the sample in the flow direction (m), S is the section of the sample (m^2) Q the volumetric flow rate ($m^3\ s^{-1}$), and μ is the dynamic viscosity of the fluid ($kg\ m^{-1}\ s^{-1}$). Permeability values are reported in Darcy units ($1\ D \approx 0.987 \times 10^{-12}\ m^2$).

2.3. X-ray microtomography

The geometry of the sample was characterized by X-ray microtomography (XMT) at the European Synchrotron Radiation Facility ID19 beamline (Grenoble, France). The XMT method is based on a 3D reconstruction from a thousand 2D radiographs of the X-ray attenuation properties of the various materials forming an object. As air and calcite in the rock have different elemental compositions with distinct atomic mass, their attenuation properties are different. Therefore, they can easily be differentiated on the radiographs, and thus on the 3D images. However, the two calcite phases (i.e. micrite and sparite) are not clearly distinguishable because they have approximately the same density and chemical composition.

The optical system used in the experiment provides a spatial resolution of 4.91 μm (pixel size) for an optical resolution of 6 μm. One thousand and two hundred projections (radiographs) of the sample were taken every 0.15° for an angle θ ranging from 0 to 180°, as the specimen sat on a rotation stage. Three data sets were collected, before the experiment (time t_0), after 9 h of the flow-through experiment (t_1) and at the end of the experiment, i.e. after 15 h (t_2). As the camera field is shorter than the height of the sample, only the upper part close to the inlet was scanned. Volume reconstruction was done with a back-projection algorithm (Herman, 1980). The reconstruction provides 3D images of the X-ray absorption by the different materials in the sample. Each data set is $2048 \times 2048 \times 1728$ voxels. A voxel is defined as a pixel cubed and is represented as a volume of $4.91 \times 4.91 \times 4.91\ \mu m^3$. A more detailed description of the XMT acquisition procedure and image processing can be found in Noiriel et al. (2007).

2.4. Analysis of 3D geometry with X-ray microtomography

By using appropriate image processing it is possible to accurately quantify parameters characterizing the sample geometry, i.e., porosity distribution, pore connectivity and geometric surface area of the fluid–rock interface. To do this, the images must be segmented, i.e. the voxels belonging to the pore space must be distinguished from those belonging to the solid matrix. As data are noisy, a simple segmentation based on a threshold value would lead to significant errors. Thus, a segmentation technique based on region growing was preferred (Gonzales and Woods, 1992). Before the segmentation procedure, the data sets were normalized through a linear interpolation procedure to achieve consistency within a dynamic range of intensity values on the different images. The noise was reduced by running a 3D median filter. Then, the different parameters for segmentation were chosen by visual inspection of the grey-level histogram, and the results were validated by comparison of the segmented volumes with the grey-scale ones. During the whole segmentation procedure, the parameters were kept constant for each data set to ensure a better representativeness of the results.

After segmentation, the total porosity of the sample ϕ is simply the ratio of the pore space to the total number of voxels. The local porosity $\phi(z)$ can also be calculated for each slice along the flow axis. The surface area (m^2) of the porous medium is defined as the number of fluid–rock edge pixels N_{pix} multiplied by the pixel surface area ($S_{pix} = 4.91 \times 4.91\ \mu m^2$). The geometric surface area normalized to the volume of the porous medium is defined by:

$$S_{geo} = \sum_{V_T} N_{pix} \times S_{pix} / V_T \quad (7)$$

with V_T the volume of the sample. Here, S_{geo} ($m^2\ m^{-3}$) denotes the geometric surface area of both connected and non-connected pores for micrite and sparite. The geometric surface area used in numerical models is often expressed as a function of the mineral volume (or mass) or of the pore volume. The geometric surface area is related to the pore volume by:

$$S^*_{geo} = \sum_{V_T} N_{pix} \times S_{pix} / (\phi \times V_T) \quad (8)$$

with S^*_{geo} in $m^2\ m^{-3}$.

2.5. Measurement of major and minor elements by ICP-AES and ICP-MS

Concentrations of Ca, Mg, Na, K and Si in the outlet solution were measured by inductively coupled plasma atomic emission spectroscopy (ICP-AES), whereas Ba, Li, B, Mn, Rb elemental compositions were measured by inductively coupled plasma mass spectroscopy (ICP-MS). Concentrations of Sr were measured either by ICP-AES or by ICP-MS. Aqueous samples were acidified with nitric acid ($pH < 2$) prior to analysis. Calibration standards were prepared from commercial stock solutions. Sample spike and replicate analyses were performed to ensure accuracy and precision of the analyses. The calibration was verified continuously with a standard solution to monitor the instrument performance. The accuracy of the measurements is less than 2%.

The porosity changes were estimated from Ca amounts removed by the fluid flowing through the sample. Because the rock consists almost entirely of calcite, the porosity at time t_i is given by:

$$\phi_{Ca}(t_i) = \phi_0 + \left(Q \times {}_{v_{cal}} / V_T\right) \int_{t=t_0}^{t=t_i} \Delta Ca\ dt \quad (9)$$

with ϕ_{Ca} the sample porosity calculated from chemical analyses, ϕ_0 the initial sample porosity (at t_0), v_{cal} the molar volume of calcite ($m^3\ mol^{-1}$), ΔCa the variation in calcium concentration between the inlet and the outlet of the sample ($mol\ m^{-3}$). The chemical flux ($mol\ s^{-1}$) of the species C_i released by the sample is given by:

$$F_{C_i} = Q \times \Delta C_i \quad (10)$$

Table 1
Chemical data on micrite and sparite calcites from SIMS analysis.

Sample and analysis	C	B	Mg	Ca	Mn	Fe	Sr	Ba
Sparite-1	129,446.64	–	6308.83	393,460.45	–	–	1223.02	11.81
Sparite-2	129,146.43	23.94	5115.38	394,737.87	186.50	3013.43	1461.73	9.00
Sparite-3	146,558.82	26.70	6292.36	388,559.84	187.52	5202.31	1088.08	11.68
Sparite-4	–	–	–	400,800.00	–	–	1309.77	12.39
Sparite-5	126,963.06	24.27	5423.77	390,418.64	113.66	4300.19	997.43	12.39
Micrite-1	154,828.34	95.72	9449.26	377,907.61	202.58	12,718.91	134.65	26.70
Micrite-2	142,574.16	169.25	13,236.91	366,578.34	225.79	20,158.86	154.90	40.18
Micrite-3	137,525.12	77.28	10,604.31	374,339.86	173.09	15,110.50	115.98	29.94

Data are in ppm.
– means no measurement.

with ΔC_i the variation in C_i concentration between the inlet and the outlet of the sample (mol m^{-3}).

2.6. Secondary ion mass spectroscopy and ion microprobe analysis

The distribution of the minor element (Mg) and trace elements (B, Mn, Fe, Sr, and Ba) in the micrite grains and the sparite cement was determined by secondary ion mass spectrometry (SIMS) technique, using a Cameca IMS6f instrument. Sputterization of a gold-coated sample by a primary beam of $^{16}O^-$ ions yields secondary ions which are analysed in the mass spectrometer. The primary beam is accelerated by a total field of 17 kV for a total intensity of around 100 nA, and rastered over a 50×50 µm wide surface, resulting in a flat-bottomed crater in the analysed area. Secondary ions collected through the immersion lens are subsequently filtered in position using a transfer lens and field aperture settings. The resulting analysed area is 15 µm in diameter. Isobaric polynuclear interferences are resolved by using high-energy ions (120 eV for $^{44}Ca^+$ and $^{88}Sr^+$; 60 eV for $^{11}B^+$, $^{12}C^+$, $^{26}Mg^+$, $^{55}Mn^+$, $^{54}Fe^+$, and $^{138}Ba^+$). Ion counting is performed sequentially with counting times ranging from 5 to 20 s, with 3 or 4 sequences in each analysis. A two-step data reduction process is applied to raw data. Intensity ratios with $^{44}Ca^+$as the internal standard are derived by interpolation for signal-drift correction and later transformed into atomic ratios using external standards. The elemental concentrations were computed by normalization of the sum of oxides to 100% because all major elements were analysed. The main external standard was a calcite sample (Iana9), displaying chemical heterogeneity of less than 2% for most elements (8% for iron). In addition, an aragonite grain was used as standard for C, Mg, and Sr. The composition of calcite Iana9 was determined by instrumental neutron activation analysis and its homogeneity checked by SIMS. Specifically, the boron concentration was derived from SIMS analyses by comparison with silicate glasses and must be considered as semi-quantitative. The analytical accuracy determined from counting statistics and sequence repeats ranges from 0.5–2% for B, Mg and Sr, to 2–3% for Mn and Fe and to 2–6% for Ba.

3. Results

3.1. Minor and trace element chemistry of the rock sample

SIMS analyses show that the abundance of minor and trace elements allows us to distinguish micrite from sparite, which have different chemical signatures. The partitioning of minor and trace elements between the two calcites depends on the crystallization conditions, such as temperature, precipitation rate, lattice structure of the element, growth step and various features of water composition, including ionic strength and residence time (Plummer, 1977; Reeder, 1996).

The results of the SIMS analysis of various calcite grains are presented in Table 1. Abundance of Sr, B, Fe, Mg and Ba appears particularly discriminatory between the two calcites, while Mn concentrations overlap substantially. In particular, the sparite is the one most enriched in Sr, whose concentration is 9 times higher than in micrite. The strontium is incorporated into the calcite through substitution for Ca^{2+} in the lattice (Pingitore et al., 1992), forming a dilute solid solution. On the other hand, the micrite is more enriched in B, Fe, Mg and Ba, and displays more heterogeneous distribution for all analysed elements.

The Ca concentration close to $40 \cdot 10^3$ ppm indicates a relative purity of the sparite calcite, whereas the lower abundance of Ca in the micrite suggests that this phase contains a small proportion of minerals that differ from calcite. Observations by scanning electron microscopy (SEM) show that the residues are predominantly clay minerals, which are common in micrite. Compared to calcite, some elements may be preferentially incorporated in the clay structure, because of the ionic substitutions that may occur in the octahedral and tetrahedral sheets, or in the interlayer of the clays. Energy dispersive X-ray spectroscopy (EDX) analysis indicates that the clay minerals are enriched in Fe and K. In addition, cations such as B^{3+}, Ca^{2+}, Na^+, Mg^{2+}, Ba^{2+} or Rb^{2+} can also be found in the interlayer (Velde, 1995; Meunier, 2005). It is worth noting that Ba may be ubiquitous in calcite and clay minerals, but it is not possible to measure its concentration in each mineral.

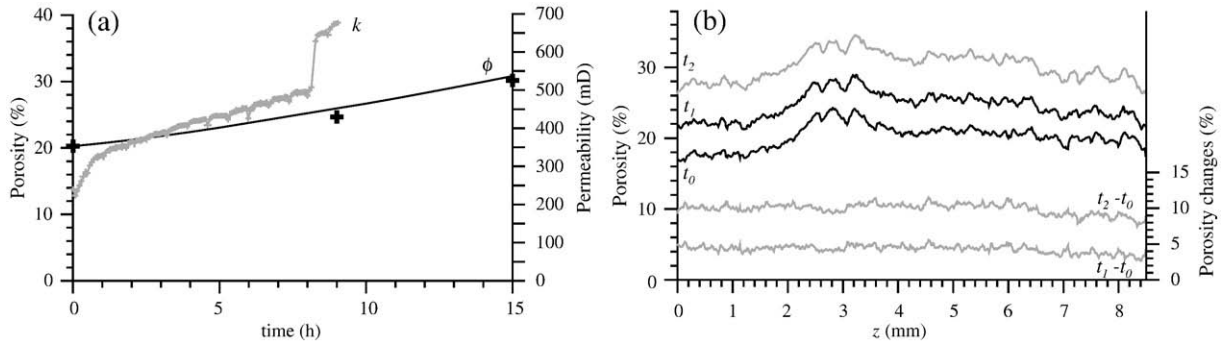

Fig. 4. (a) Permeability (k), total porosity (ϕ) measured from fluid chemistry (black solid line) and by XMT (crosses) with time, and (b) Average porosity along the flow direction axis z, at times t_0, t_1 and t_2, and porosity difference between t_1 and t_0 ($t_1 - t_0$), and t_2 and t_0 ($t_2 - t_0$).

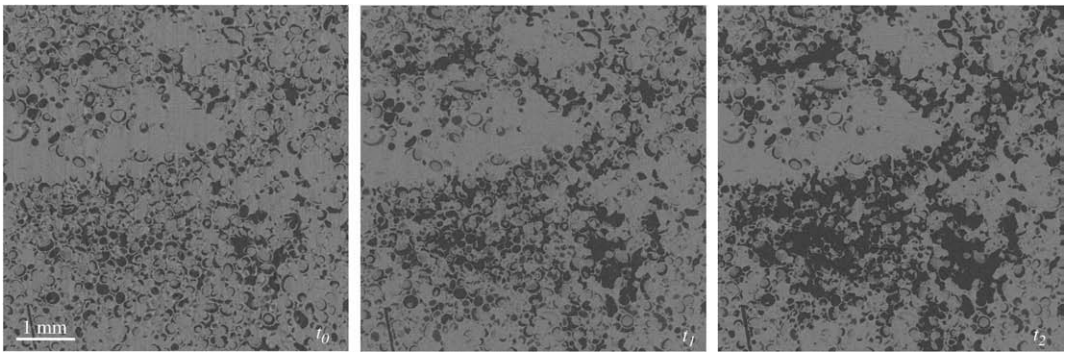

Fig. 5. XMT cross-section of the sample at t_0, t_1 and t_2 ($z = 1.02$ mm).

The minor and trace elements are incorporated into calcite to form a solid solution. Some of these elements can be helpful to discriminate between the relative contribution of sparite and micrite throughout the global dissolution process (see Section 3.4.2). However, two conditions are required for these elements to be considered as good tracers: (1) they have to be present only in the calcite lattice, which excludes elements that can be incorporated mainly in the minor clay (e.g. Rb or B) or oxide (e.g. Fe or Mn) fraction; (2) their amount must be highly different between micrite and sparite. The best elements that allow to distinguish micrite from sparite are Sr, which is in average 9 times higher in sparite than in micrite, and Ba, which is in average 2.8 times higher in micrite than in sparite. Assuming in a first approach that Ca, Sr and Ba exist only in the calcite lattice, the two calcites can be defined as calcite–$SrCO_3$–$BaCO_3$ solid solutions with the formula: $(Ca_{1-x-y}, Sr_x, Ba_y)CO_3$. Then, the composition of the two calcites is determined, i.e. $Ca_{0.998585}Sr_{0.001407}Ba_{0.000008}CO_3$ for sparite, and $Ca_{0.999809}Sr_{0.000166}Ba_{0.000025}CO_3$ for micrite.

3.2. Porosity and permeability changes

The initial porosity of the sample ϕ_0 is determined from XMT at t_0. Values of porosity calculated from the mass balance (Eq. (9)) and XMT are reported in Fig. 4a, as well as the permeability. The porosity determined by XMT increases from 20.3% at t_0, to 24.7% and 30.2% at t_1 and t_2, respectively. The XMT-measured porosity is in good agreement with the porosity calculated from the mass balance, which reaches 25.3% and 29.7% at t_1 and t_2, respectively. The local porosity change along the flow axis is also computed, by calculating averaged porosity for each 3D image cross-section normal to the flow direction (Fig. 4b). As shown in Fig. 5, dissolution occurs in areas where the pore connectivity is the highest, and the variable porosity distribution reflects the spatial heterogeneities initially present in the rock. In addition, porosity changes are not evenly distributed, and the porosity increase is slightly higher near the sample inlet (Fig. 4b). Indeed, both the saturation index and the pH increase in the sample as the reaction progresses toward equilibrium, and the dissolution rate of calcite progressively decreases, which explains why the porosity increase is higher close to the inlet.

The permeability increases from 220 to 680 mD between t_0 and t_1. The increase is stronger at the beginning of the experiment and becomes more progressive. A large increase is observed after 8.5 h of experiment, probably indicating the breakthrough of the dissolution front. A great permeability increase is also observed during the re-saturation of the sample after t_1, which is probably due to sample damage. Thus, the precision of the sensors did not enable to measure k between t_1 and t_2. Micrite grain unhooking and displacement was, in fact, observed in some pores.

3.3. Solution chemistry

The chemical composition of the outlet solution is directly related to the relative contribution to the dissolution process by the sparite and the micrite. The temporal evolution of the concentrations in the outlet solution during the dissolution experiment is presented in Table 2. The outlet solution concentrations change with time according to two distinct trends. The concentrations of dissolved Ca, Mg and Sr increase throughout the experiment, whereas the concentrations of Ba and Rb decrease (Fig. 6). The pH rises to 5.6 ± 0.1 at the sample outlet. The outlet solution remains highly undersaturated with respect to calcite; the saturation index of calcite Ω_{cal} calculated using CHESS (van der Lee, 1998) from the Ca concentration at the sample outlet varies between -2.4 and -1.8.

Table 2
Outlet solution concentrations as a function of time.

t (h)	Ca	Mg	Sr	Ba	Mn	Na	K	Li	B	Rb
1	–	–	2.25×10^{-7}	1.23×10^{-8}	5.56×10^{-8}	–	–	2.67×10^{-8}	2.39×10^{-8}	$3.24\cdot10^{-9}$
2	1.17×10^{-3}	2.19×10^{-5}	2.48×10^{-7}	–	–	9.65×10^{-3}	1.25×10^{-4}	–	–	–
3	–	–	3.17×10^{-7}	8.66×10^{-9}	7.67×10^{-8}	–	–	1.33×10^{-8}	1.19×10^{-8}	2.64×10^{-9}
4	1.41×10^{-3}	2.37×10^{-5}	4.28×10^{-7}	–	–	9.85×10^{-3}	1.23×10^{-4}	–	–	–
5	–	–	5.27×10^{-7}	8.11×10^{-9}	8.54×10^{-8}	–	–	1.23×10^{-8}	1.25×10^{-8}	2.41×10^{-9}
6	1.64×10^{-3}	2.56×10^{-5}	7.10×10^{-7}	–	–	9.61×10^{-3}	1.15×10^{-4}	–	–	–
7	–	–	8.64×10^{-7}	7.62×10^{-9}	9.58×10^{-8}	–	–	1.58×10^{-8}	9.95×10^{-9}	2.46×10^{-9}
8	1.69×10^{-3}	2.63×10^{-5}	9.70×10^{-7}	–	–	9.49×10^{-3}	1.03×10^{-4}	–	–	–
9	–	–	1.04×10^{-6}	7.46×10^{-9}	9.80×10^{-8}	–	–	1.59×10^{-8}	7.67×10^{-9}	2.29×10^{-9}
10	1.67×10^{-3}	2.63×10^{-5}	1.19×10^{-6}	–	–	1.00×10^{-2}	9.98×10^{-5}	–	–	–
11	–	–	1.35×10^{-6}	6.94×10^{-9}	1.52×10^{-7}	–	–	1.61×10^{-8}	8.00×10^{-9}	2.05×10^{-9}
12	1.88×10^{-3}	2.98×10^{-5}	1.50×10^{-6}			1.01×10^{-2}	9.94×10^{-5}	–	–	–
13	–	–	1.60×10^{-6}	6.53×10^{-9}	1.57×10^{-7}	–	–	2.09×10^{-8}	8.97×10^{-9}	1.84×10^{-9}
14	1.96×10^{-3}	2.98×10^{-5}	1.64×10^{-6}	–	–	9.26×10^{-3}	9.25×10^{-5}	–	–	–
15	–	–	1.89×10^{-6}	7.27×10^{-9}	1.68×10^{-7}	–	–	2.08×10^{-8}	1.17×10^{-8}	2.07×10^{-9}

Data are in mol l^{-1}.
– means no measurement.

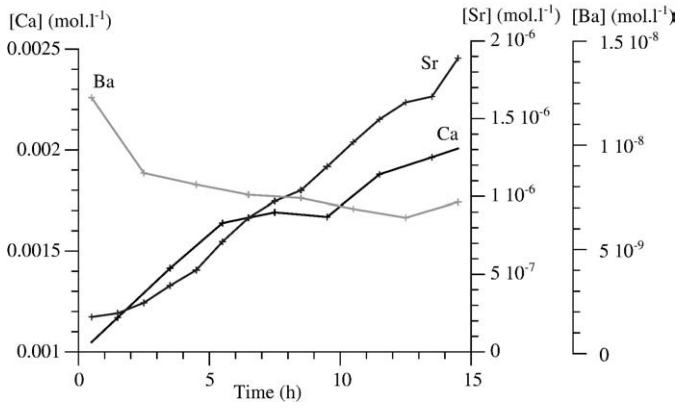

Fig. 6. Concentration of Ca, Sr and Ba at the sample outlet during the experiment.

3.4. Surface area changes

3.4.1. Geometric surface area

Measurements of the geometric surface area with XMT do not reveal any major changes in the fluid–rock interface area with time. The weak point in the XMT method is that the surface areas of micrite and sparite cannot be distinguished on the 3D images, and the geometric surface area represents the whole surface area of the void–mineral interface. The geometric surface area S^{*}_{geo} related to the pore volume decreases from 120.1 at t_0 to 94.8 and 75.4 $m^2\ l^{-1}$ at t_1 and t_2, respectively. These changes are explained by a decrease in calcite mass and an increase in the pore volume as porosity increases. The changes in geometric surface area S_{geo} are small, from 24.0 at t_0, to 23.1 and 22.5 $m^2\ l^{-1}$ at t_1 and t_2, respectively. These results indicate that the fluid–rock interface area hardly changes at all.

Observations of the XMT images reveal that the pore-size of sparite crystals increases, whereas the pore-size of micrite grains decreases (Fig. 7a,b,c). As a first approximation, micrite grains can be viewed as spheres whose radius decreases and sparite crystals as volumes surrounded by spherical pores whose radius increases (Fig. 7d). Pore smoothing and connectivity also increase, which explains why the overall geometric surface area decreases while the pore size increases.

3.4.2. Reactive surface area

An increase of Ca released at the sample outlet indicates an increase in the overall calcite dissolution rate with time. With a constant flow rate, only two mechanisms can cause changes in the concentration and flux of Ca at the sample outlet. The first one is the kinetics of calcite dissolution (Eqs. (1) and (2)), which depends on the saturation index of the solution, pH, P_{CO2}, catalyser and inhibitor effects, and reactive surface area. The second is the mass transfer of the elements, which depends on advection, dispersion and diffusion. Changes in porosity can affect transport by changing the flow paths and the local fluid velocities. However, if mass-transfer changes affected the chemical flux, the Ca, Sr and Ba concentrations would change in the same proportions. But Ca, Sr and Ba concentrations vary non-proportionally during the experiment (Fig. 6). Changes in the Sr:Ca and Ba:Ca concentration ratios in the outlet solution indicate that the dissolution rates of micrite and sparite are different in time, which cannot be attributed to mass transfer effects but to chemical processes. Assuming that the changes in porosity and permeability do not notably affect the mass transfer in the sample (i.e., the mass transfer is in steady-state) and that the two calcites theoretically obey the same kinetic dissolution law, changes in Ca and trace-element concentrations can only be attributed to changes in the reactive surface area of micrite and sparite. A decrease in Ba, B and Rb may indicate that the reactive surface area of micrite decreases, while a large increase in Sr concentration may suggest that the reactive surface area of sparite increases.

It is difficult to measure the absolute size of the reactive surface area by chemical analysis, because the rate of calcite dissolution varies as long as calcite is being dissolved in the sample and the local pH and saturation index change. Nevertheless, it is possible to determine the variations of the reactive surface area with time. The changes in Ca and

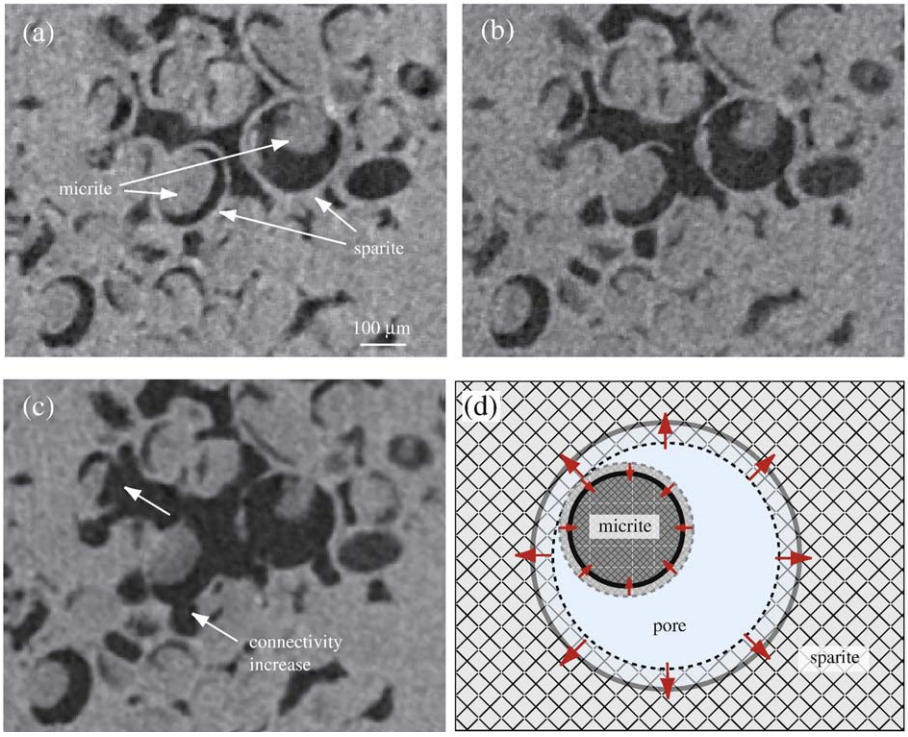

Fig. 7. (a,b,c) XMT image of the pore structure at t_0, t_1 and t_2 showing the geometry changes of the sparite and micrite grains ($z = 0.45$ mm), and (d) geometrical model of spherical surface area growth and reduction for sparite and micrite.

Sr concentrations in the outlet solution are distinctly different, denoting that the contributions by micrite and sparite to the overall dissolution differ. The proportion of micrite and sparite surface area that contributes to the chemical reaction can be deduced from the chemical composition of the two solid solutions forming the sparite and the micrite, by solving the system of equations:

$$\begin{cases} x\mathrm{Ca}_{(\mathrm{mic})} + y\mathrm{Ca}_{(\mathrm{spar})} = \mathrm{Ca}_{(\mathrm{tot})} \\ x\mathrm{Sr}_{(\mathrm{mic})} + y\mathrm{Sr}_{(\mathrm{spar})} = \mathrm{Sr}_{(\mathrm{tot})} \end{cases} \quad (11)$$

where x and y are the fraction of micrite and sparite reactive surface area involved in the chemical reaction, respectively; $\mathrm{Ca}_{(\mathrm{mic})}$, $\mathrm{Ca}_{(\mathrm{spar})}$, $\mathrm{Ca}_{(\mathrm{tot})}$ are the concentrations of calcium released by the micrite, the sparite and the outlet solution, respectively, and $\mathrm{Sr}_{(\mathrm{mic})}$, $\mathrm{Sr}_{(\mathrm{spar})}$, $\mathrm{Sr}_{(\mathrm{tot})}$ are the concentrations of strontium released by the micrite, the sparite and the outlet solution, respectively.

Results are shown in Fig. 8a. At the beginning of the experiment, the reactive surface area of the micrite contributes 96% to the reaction, for only 4% of the reactive surface area of the sparite. In other words, 96% of the calcium flux ($F_{\mathrm{Ca(tot)}}$) in the outlet solution comes from micrite dissolution, and only 4% from the sparite. The contribution by the micrite reactive surface area to the reaction decreases progressively whereas the sparite contribution increases. At the end of the experiment, the surface area of micrite contributes 37% to the reaction, for 67% of the sparite surface area. The flux of Ca from micrite $F_{\mathrm{Ca(mic)}}$ and sparite $F_{\mathrm{Ca(spar)}}$ are given by:

$$\begin{aligned} F_{\mathrm{Ca(mic)}} &= xF_{\mathrm{Ca(tot)}} \\ F_{\mathrm{Ca(spar)}} &= yF_{\mathrm{Ca(tot)}} \end{aligned} \quad (12)$$

The results are presented in Fig. 8b. Changes in fluxes are directly related to the changes in the reactive surface area of micrite and sparite. $F_{\mathrm{Ca(mic)}}$ increases during 5 h and then decreases, indicating that the changes in reactive surface area of micrite are parabolic in time. $F_{\mathrm{Ca(spar)}}$ increases continuously after 1 h of the experiment, from 1.16×10^{-9} to 3.49×10^{-8} mol s^{-1}, indicating a large increase in the reactive surface area of sparite.

4. Numerical modelling of reactive transport

A numerical model was used to resolve the reactive transport problem discussed above, by integrating a quantitative analysis of the reactive surface area changes. The simulations were performed using HYTEC, a reaction-transport numerical code (van der Lee et al., 2003). The code is based on the resolution of coupled equations describing mass conservation and solute transport. It provides feedback on the influence of porosity changes on permeability, reactive surface area and diffusion coefficient changes. Possible chemical reactions include surface complexation, cation exchange, and precipitation/dissolution of minerals (in equilibrium or according to kinetic laws). Different surface models (Eqs. (3)–(5)) are used to investigate the effects of variable reactive surface areas on reactive transport.

The system consists of a one-dimensional parallelepiped column, 15 mm in length, representing the limestone sample. The column is discretized into 15 regularly spaced grid blocks. The volume of the column is set at that of the cylindrical sample (954 mm^3). Thus, the domain has a dimension of 15×0.064 mm^2 ($\times1$ m in the third dimension). A flux-segment is defined at the outlet of the column in order to calculate the chemical flux F_{c_i} (mol s^{-1}) of the different species through the surface of the modelled domain.

The column represents a porous limestone with a porosity of 20.3% and a hydraulic conductivity of 2.2×10^{-3} m s^{-1}. The limestone is composed of two different calcite solid solutions with the chemical compositions of micrite and sparite (see Section 3.1). The two calcite–$SrCO_3$–$BaCO_3$-minerals are introduced into the CTDP thermodynamic database (Common Thermodynamic Database Project, van der Lee and Lomenech, 2004; van der Lee, 2004, http://www.ctdp.org. The thermodynamic equilibrium constant of these new minerals is set equal to the calcite equilibrium constant, as the two solid solutions have low Sr and Ba contents. This assumption is valid under highly undersaturated conditions, while dissolution of the calcite solid solution is congruent, i.e., one mole of dissolved (Ca_{1-x-y}, Sr_x, Ba_y) CO_3 mineral produces $1-x-y$, x, and y moles of Ca, Sr and Ba, respectively. An artificial, non-reactive tracer is also added to each of the two calcites to distinguish the concentrations of Ca, Sr and Ba released by the micrite from those released by the sparite during congruent dissolution of the two solid solutions. The tracer does not affect the thermodynamic equilibrium or kinetic laws.

The initial fluid in the column is in equilibrium with calcite at atmospheric partial pressure of CO_2 ($P_{CO2}=10^{-4.5}$ MPa, pH = 8.32). The inlet fluid is water + 0.01 M NaCl equilibrated with 1 bar partial pressure of CO_2 ($P_{CO2}=0.1$ MPa). The fluid is injected at a constant flow rate ($Q=100$ cm^3 h^{-1}), corresponding to a Darcy flux boundary condition of 4.4×10^{-4} m s^{-1} at the column inlet. Consequently the system is highly advective. The diffusion coefficient of the aqueous species is 7.9×10^{-10} m^2 s^{-1}, which corresponds to the diffusion coefficient of Ca^{2+} in water (Li and Gregory, 1974). The longitudinal dispersivity is set at 0.1 mm.

Mineral dissolution is considered kinetically constrained (Eq. (1)). The kinetic-rate formulation by Plummer et al., 1978) in Eq. (2) is used for both micrite and sparite. The changes in reactive surface area of micrite and sparite were modelled. A total of three simulations were

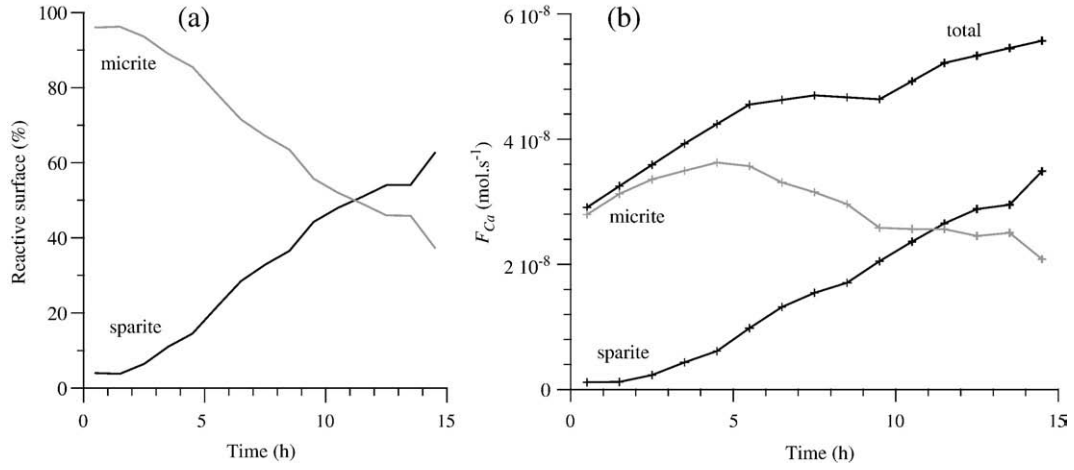

Fig. 8. (a) Variation of reactive surface areas (percentage) of micrite and sparite that are reactive within the sample during the experiment, and (b) total calcium flux released by the sample and calcium flux from micrite and sparite.

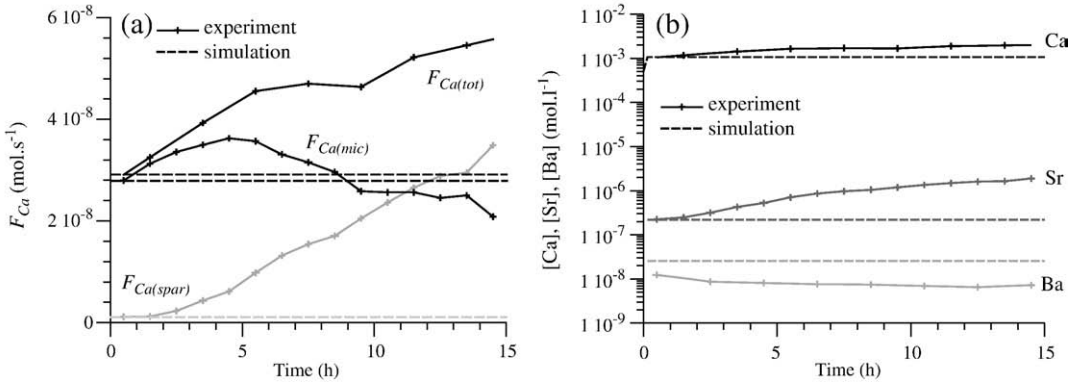

Fig. 9. (a) Flux of Ca, and (b) Ca, Sr and Ba concentrations at the sample outlet using the constant surface area model.

carried out with different reactive surface models. The first model represents a constant reactive surface area. The second one is based on spherical grain reduction and spherical pore growth (Eqs. (3) and (4)). The third is a "sugar-lump" model (Eq. (5)). The simulations are run for 15 h. In order to check the effects of reactive surface area changes, the porosity and permeability are kept constant during the simulations in order to separate the effect of reactive surface area changes from the possible feedback effect due to porosity and permeability changes. A first attempt is to reproduce the available experimental observations, i.e. the composition of the solution at the outlet, the chemical flux and the variation of reactive surface area for both micrite and sparite.

4.1. Constant-surface area model

The first simulation was run assuming that micrite and sparite have constant reactive surface areas. In order to fit the experimental concentration and flux at the beginning of the flow-through experiment, the size of reactive surface area S_{r0} was initially adjusted to 6.50 $m^2\,l^{-1}$ for micrite and 0.25 $m^2\,l^{-1}$ for sparite. As determined from the experiment, micrite represents 96% of the total surface area and sparite 4%. Because the limestone consists of 60% micrite and 40% sparite (see Section 2.1), the reactive surface area normalized to the mineral volume is equal to 5.42 $m^2\,l^{-1}$ and 0.31 $m^2\,l^{-1}$ for micrite and sparite, respectively.

Results are presented in Fig. 9. Initial concentrations and flux are well reproduced for Ca and Sr, but overestimated for Ba. However, Ba cannot be considered as a reliable tracer of the calcite dissolution in the micrite, because a significant amount of Ba can be associated with the clays, whose dissolution rate is about 10^{-6} times lower than that of calcite under acidic conditions (Köhler et al., 2003). Consequently, micrite may contain less Ba in the calcite lattice than previously assumed (see Section 3.1).

Steady-state dissolution rates are achieved rapidly because the reactive surface area neither increases nor decreases with dissolution. As a result, the concentrations and fluxes are constant with time. Thus, the constant-surface area model is unable to reproduce the experimental observations.

4.2. Spherical-grain-and-pore model

The second simulation was run under the hypothesis that micrite can be approximated by spherical grains and sparite by crystals surrounding spherical pores. The size of the reactive surface area is initially kept at 6.5 $m^2.l^{-1}$ for micrite and 0.25 $m^2.l^{-1}$ for sparite. Eqs. (3) and (4) describe the changes in reactive surface area of the spherical micrite grains and the spherical pores surrounding the sparite, respectively. The reactive surface area of micrite decreases as dissolution occurs, whereas the reactive surface area of micrite increases. As shown in Fig. 10, this geometrical model also fails to reproduce the experimental results. The decrease in micrite and increase in sparite reactive surface areas are both too weak. As the participation of the micrite surface area is dominant in the overall reaction, Ca and Sr concentrations at the outlet decrease continuously instead of rising.

4.3. Sugar-lump model

A best fit of the measured Ca and Sr concentrations and flux is obtained by the sugar-lump model. The size of the reactive surface area is initially the same as previously. Coefficients S_{rm}, n_1, n_2 and n_3 in Eq. (5) are equal to 29, 1.0, 2.0, 0.9 for sparite and to 9.0, 0.8, 5.0, 1.7 for micrite, respectively. The results, presented in Fig. 11, are in good

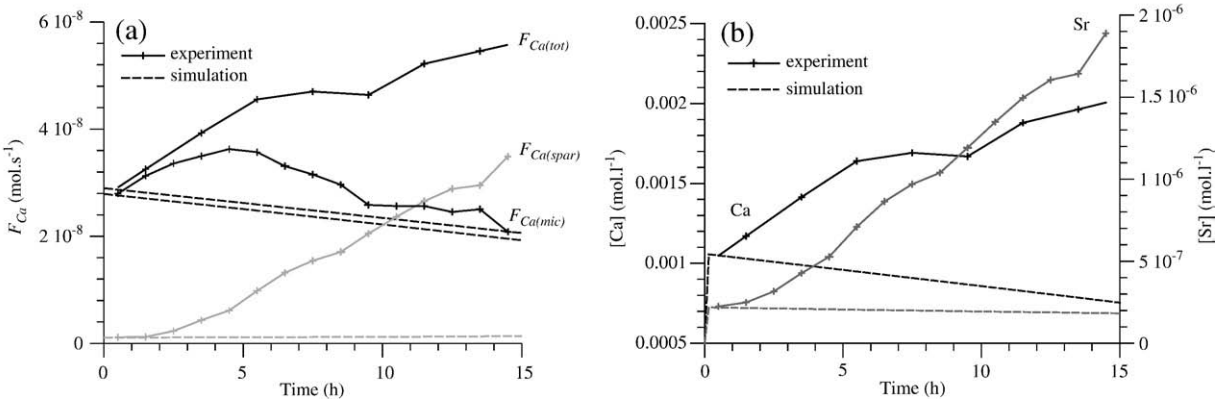

Fig. 10. (a) Flux of Ca, and (b) Ca and Sr concentrations at the sample outlet using the spherical-grain-and-pore model.

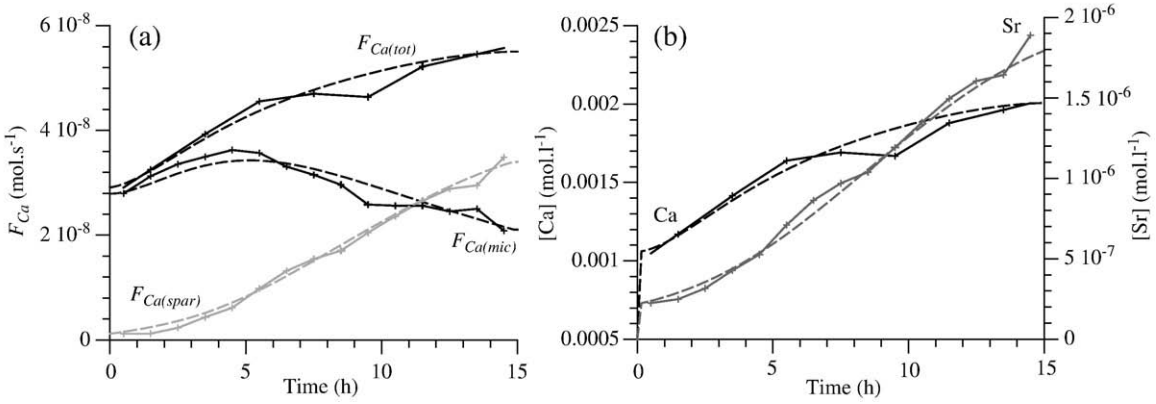

Fig. 11. (a) Flux of Ca, and (b) Ca and Sr concentrations at the sample outlet using the sugar-lump model.

agreement with the experimental Ca and Sr concentrations at the sample outlet, even if second-order variations cannot be reproduced. The reactive surface area of the two calcites doubles during the experiment, from 6.75 m^2 l^{-1} (t_0) to 12 m^2 l^{-1} (t_2). The micrite reactive surface area first increases from 6.5 to 8 m^2 l^{-1}, and subsequently decreases to 5 m^2 l^{-1}. The sparite reactive surface area increases from 0.25 to 7 m^2 l^{-1}. The sugar-lump model is able to reproduce the large increase in reactive surface area of sparite and the parabolic variation in reactive surface area of micrite.

5. Discussion

The micrite reactive surface area is 17 times greater than that of sparite at the beginning of the experiment. This difference may stem from the grain size in the two calcites (Fig. 2b): the smaller the grain size, the higher the reactive surface area (Hodson, 2006). Moreover, the micrite displays higher interparticle micro-porosity than the sparite, so that the surface area in contact with the fluid may be larger.

There is a great difference between the geometric surface areas measured by XMT and the reactive surface areas determined from chemistry. For instance, the reactive surface area of both calcites doubles during the experiment, whereas the geometric surface area decreases. It is not surprising that S_r and S^*_{geo} are different, because, generally, the whole surface area is not reactive. However, it was not expected that S^*_{geo} would be higher than S_r. There are two possible reasons for this difference. Firstly, the fact that XMT is used here to measure the whole surface area of the pores (i.e. surface area of both connected and unconnected pores), which is greater than the surface area in contact with the flowing aqueous phase. Although a method has already been developed to distinguish a reactive from a non-reactive surface area in the use of XMT (Noiriel et al., 2005), the procedure involves a precise 3D registration of the different images in a common coordinate system. In this study, the method failed to give accurate results because of the strong rock heterogeneity. Secondly, XMT is not able to capture the geometry at the micro-scale because of its weak spatial resolution. Thus, the individual sparite and micrite crystals, the grain boundaries and the micro-porosity are not distinguishable on the images. Processes responsible for reactive-surface area changes may be active at a scale which is smaller than what can be measured with a resolution of about 5 µm using XMT.

Reactive transport simulations demonstrated that the spherical-grain-and-pore model failed to describe the experiment, whereas the sugar-lump model produced the best fit of the experimental data. The spherical-grain-and-pore model was unable to reproduce the large changes in the reactive surface areas of micrite and sparite, while this model seems to be more realistic in representing the mineral distribution within the rock using XMT (Fig. 5). Colon et al. (2004) also reported a greater increase in reactive surface area than predicted with a geometric model of packed spheres during a Fontainebleau sandstone dissolution experiment. The authors attributed the differences to the roughness of the quartz grains and the opening of new pore voids. Despite the smoothing of the euhedral sparite crystals observed in our experiment, which aims at decreasing S_r, the substantial increase in pore connectivity may explain the observed large increase. The connectivity increase can be observed at two scales: (1) between two pores (Fig. 5) and (2) inside a pore. Indeed, the micro-porous boundaries between sparite crystals can be progressively invaded by the flowing fluid as dissolution occurs, thus progressively dislocating the crystals and increasing the reactive surface area. Taking this process into consideration, the sugar-lump theory appears well suited to describing the dissolution process in both micrite and sparite (Fig. 1) when the processes are studied at the micron scale.

6. Conclusion

The relation between the increasing dissolution rate of two types of calcite, namely micrite grains and sparite crystals, and the time of chemical alteration was investigated in a porous limestone during an acidic water flow-through experiment. Measurements of some minor and trace elements both in the minerals and the outlet solution appear to be useful to better understand the fluid–rock interactions in multi-mineral rocks. The results show the kinetic control exerted by the calcite reactive surface area of the overall dissolution rate, while the permeability increase and flow localisation seem to have negligible effects on the mass transfer process within the rock.

The calcite grain size, the mineral spatial distribution and the pore connectivity strongly influence the reactive surface area changes during the dissolution experiment. The Damköhler number can also certainly influence the geometric surface area by influencing the size and number of new dissolution pathways that were developed within the sample. The micrite reactive surface area exhibits parabolic changes, whereas that of sparite greatly increases with time. Although a geometric surface area determined by XMT and one determined from chemistry measurements are different and not correlated, the XMT method is useful for observing geometry changes and interpreting the experimental results.

The results underline the problem of the applicability of geometrical models to computing surface area changes in natural systems. Predictions based on ideal spherical-grain and spherical-pore geometries fail to reproduce experimental data, even if this model seems to give the best representation of the porous sample geometry at the scale of XMT observation. Processes responsible for reactive surface area changes may act at a scale smaller than what can be measured with the XMT resolution. A good fit of the experimental data is obtained with a sugar-lump model. The sugar-lump representation is coherent with

the SEM observations at the microscopic scale. Boundaries between sparite crystals, whose surface area is not measurable with XMT, can greatly increase the reactive surface area as fluid progressively invades the initially non-connected porous network.

This study highlights the need for future experimental and numerical studies in the field of reactive transport. The results have important implications for the interpretation and modelling of reactive surface area changes during reactive transport. They suggest that the variations in reactive surface area of minerals can significantly influence the reactive transport properties within a rock, but these variations are more complex than what might be deduced from a simplified geometric assemblage. However, this experiment constitutes only a first step with limitations on sample scale and time duration inherent to laboratory experiments. It would be interesting to follow reactive transport and reactive surface area changes on the long range, particularly close to the equilibrium, where calcite precipitation can be expected. The upscaling of reactive surface areas from the microscopic to the macroscopic scale remains also a matter of debate. The next step is connecting microscopic scale reactive transport modelling to the XMT data, in order to quantify the effective surface of reaction (Noiriel et al., 2004), since surface area distributed along major flow pathways will be more important than surface area in either disconnected pores or in smaller pathways that do not accommodate as much fluid flow, i.e. where diffusive transport is dominant compared to advection.

Acknowledgments

Funding for this work was provided through the European Commission contract RDG (EKV-2001-00091 Alliance) and the French ministry of Research (MENRT Grant to C. Noiriel). Use of the European Synchrotron ID19 Source was supported by the EU under project ME680. S. Pourtalès and C. Nevado (University of Montpellier) are thanked for their assistance with ICP-MS and preparation of thin sections. The reviewers are also thanked for their constructive comments and contributions.

References

Bachu, S., Adams, J.J., 2003. Sequestration of CO_2 in geological media in response to climate change: capacity of deep saline aquifers to sequester CO_2 in solution. Energy Convers. Manag. 44 (20), 3151–3175.
Bernard, D., 2005. 3D quantification of pore scale geometrical changes using synchrotron computed microtomography. Oil Gas Sci. Technol. 60 (5), 747–762.
Brosse, E., Magnier, C., Vincent, B., 2004. Modelling fluid–rock interaction induced by the percolation of CO_2-enriched solutions in core samples: the role of reactive surface area. Oil Gas Sci. Technol. 60 (2), 287–306.
Brunauer, S., Emmet, P.H., Teller, E.A., 1938. Adsorption of gases in multimolecular layers. J. Am. Chem. Soc. 60, 309–319.
Canals, M., Meunier, J.D., 1995. A model for porosity reduction in quartzite reservoirs by quartz cementation. Geochim. Cosmochim. Acta 59 (4), 699–709.
Colon, C.F.J., Oelkers, E.H., Schott, J., 2004. Experimental investigation of the effect of dissolution on sandstone permeability, porosity, and reactive surface area. Geochim. Cosmochim. Acta 68 (4), 805–817.
Daccord, G., Lietard, O., Lenormand, R., 1993. Chemical dissolution of a porous medium by a reactive fluid: 1. Model for the wormholing phenomenon. Chem. Eng. Sci. 48 (1), 169–178.
Emmanuel, S., Berkowitz, B., 2005. Mixing-induced precipitation and porosity evolution in porous media. Adv. Water Resour. 28 (4), 337–344.
Flukiger, V., Bernard, D., 2009. A new numerical model for pore scale dissolution of calcite due to CO_2 saturated water flow in 3D realistic geometry: Principles and first results. Chem. Geol. 265 (1–2), 171–180 (this issue).
Fogler, H.S., Rege, S.D., 1987. Network model for straining dominated particle entrapment in porous media. Chem. Eng. Sci. 42, 1553–1564.
Fredrich, J.T., Greaves, K.H., Martin, J.W., 1993. Pore geometry and transport properties of Fontainebleau sandstone. Int. J. Rock Mech. Min. Sci. Geomech. Abstr. 30 (7), 691–697.
Fredrich, J.T., Digiovanni, A.A., Noble, D.R., 2006. Predicting macroscopic transport properties using microscopic image data. J. Geophys. Res. 111 (B3). doi:10.1029/2005JB003774.
Gautier, J.M., Oelkers, E.H., Schott, J., 2001. Are quartz dissolution rates proportional to BET surface areas? Geochim. Cosmochim. Acta 65 (7), 1059–1070.
Glassley, W.E., Simmons, A.M., Kercher, J.R., 2002. Mineralogical heterogeneity in fractured, porous media and its representation in reactive transport models. Appl. Geochem. 17 (6), 699–708.
Golfier, F., Zarcone, C., Bazin, B., Lenormand, R., Lasseux, D., Quintard, M., 2002. On the ability of a Darcy-scale model to capture wormhole formation during the dissolution of a porous medium. J. Fluid Mech. 457, 213–254.
Gonzales, R.C., Woods, R.E., 1992. Digital Image Processing. Addison-Wesley Publishing Compagny, Reading, Massachusetts. 716 pp.
Helgeson, H.C., Murphy, W.M., Aagaard, P., 1984. Thermodynamic and kinetic constrains on reaction rates among minerals and aqueous solutions. II. Rate constants, effective surface area and the hydrolysis of feldspar. Geochim. Cosmochim. Acta 48 (12), 2405–2432.
Herman, G.T. (Ed.), 1980. Image Reconstruction from Projections: Fundamentals of Computerized Tomography. Academic Press, New York. 316 pp.
Hodson, M.E., 2006. Does reactive surface area depend on grain size? Results from pH 3, 25 °C far-from-equilibrium flow-through dissolution experiments on anorthite and biotite. Geochim. Cosmochim. Acta 70 (7), 1655–1667.
Hoefner, M.L., Fogler, H.S., 1998. Pore evolution and channel formation during flow and reaction in porous media. AIChE J. 34 (1), 45–53.
Holloway, S., 1997. An overview of the underground disposal of carbon dioxide. Energy Convers. Manag. 38, 103–108.
Jamtveit, B., Yardley, B.W.D. (Eds.), 1997. Fluid Flow and Transport in Rocks: Mechanisms and Effects. Chapman and Hall, London. 319 pp.
Kaufmann, G., Braun, J., 1999. Karst aquifer evolution in fractured rocks. Water Resour. Res. 35 (11), 3223–3238.
Köhler, S., Dufaud, F., Oelkers, E.H., 2003. An experimental study of illite dissolution rates as a function of pH from 1.4 to 12.4 and temperature from 5 to 50 °C. Geochim. Cosmochim. Acta 67, 3583–3594.
Lasaga, A.C., Kirkpatrick, R.J. (Eds.), 1981. Kinetics of Geochemical Processes. . Reviews in Mineralogy, vol. 8. Mineralogical Society of America, Washington DC. 398 pp.
Le Gallo, Y., Bildstein, O., Brosse, E., 1998. Coupled reaction-flow modeling of diagenetic changes in reservoir permeability, porosity and mineral composition. J. Hydrol. 209, 366–388.
Li, Y.H., Gregory, S., 1974. Diffusion of ions in sea water and deep-sea sediments. Geochim. Cosmochim. Acta 38, 703–714.
Li, L., Peters, C.A., Celia, M.A., 2007. Effects of mineral spatial distribution on reaction rates in porous media. Water Resour. Res. 43 (1). doi:10.1029/2005WR004848.
Li, L., Steefel, C.I., Yang, L., 2008. Scale dependence of mineral dissolution rates within single pores and fractures. Geochim. Cosmochim. Acta 72 (2), 360–377.
Lichtner, P.C., 1988. The quasi-stationary state approximation to coupled mass transport and fluid–rock interaction in a porous medium. Geochim. Cosmochim. Acta 52, 143–165.
Lichtner, P.C., Steefel, C.I., Oelkers, E.H. (Eds.), 1997. Reactive Transport in Porous Media. Mineralogical Society of America, Washington DC. 438 pp.
Lüttge, A., Winkler, U., Lasaga, A.C., 2003. An interferometric study of dolomite dissolution: a new conceptual model for mineral dissolution. Geochim. Cosmochim. Acta 67 (6), 1099–1116.
Meile, C., Tuncay, K., 2006. Scale dependence of reaction rates in porous media. Adv. Water Resour. 29 (1), 62–71.
Meunier, A. (Ed.), 2005. Clays. Springer, Berlin. 472 pp.
Noiriel, C., Gouze, P., Bernard, D., 2004. Investigation of porosity and permeability effects from microstructure changes during limestone dissolution. Geophys. Res. Lett. 31 (24), L24603. doi:10.1029/2004GL021572.
Noiriel, C., Bernard, D., Gouze, P., Thibaut, X., 2005. Hydraulic properties and microgeometry evolution in the course of limestone dissolution by CO_2-enriched water. Oil Gas Sci. Technol. 60 (1), 177–192.
Noiriel, C., Madé, B., Gouze, P., 2007. Impact of coating development on the hydraulic and transport properties in argillaceous limestone fracture. Water Resour. Res. 43, W09046. doi:10.1029/2006WR005379.
Pingitore, N.E., Lytle, F.W., Davies, B.M., Eastman, M.P., Eller, P.G., Larson, E.M., 1992. Mode of incorporation of Sr^{2+} in calcite — determination by X-ray absorption-spectroscopy. Geochim. Cosmochim. Acta 56 (4), 1531–1538.
Plummer, L.N., 1977. Defining reactions and mass transfer in part of the Floridan aquifer. Water Resour. Res. 13, 801–812.
Plummer, L.N., Wigley, T.M.L., Parkhurst, D.L., 1978. The kinetics of calcite dissolution in CO_2–water systems at 5° to 60 °C and 0.0 to 1.0 atm CO_2. Am. J. Sci. 278, 179–216.
Reeder, R.J., 1996. Interaction of divalent cobalt, zinc, cadmium, and barium with the calcite surface during layer growth. Geochim. Cosmochim. Acta 60 (9), 1543–1552.
Renard, F., Gratier, J.P., Ortoleva, P., Brosse, E., Bazin, B., 1998. Self-organization during reactive fluid flow in a porous medium. Geophys. Res. Lett. 25 (3), 385–388.
Schechter, R.S., Gidley, J.L., 1969. The change in pore size distribution from surface reactions in porous media. AIChE J. 15, 339–350.
Shiraki, R., Rock, P.A., Casey, W.H., 2000. Dissolution kinetics of calcite in 0.1 M NaCl solution at room temperature: an atomic force microscopic (AFM) study. Aquat. Geochem. 6, 87–108.
Steefel, C.I., Lasaga, A.C., 1990. Evolution of dissolution patterns: permeability change due to coupled flow and reaction. In: Melchior, D., Bassett, R.L. (Eds.), Chemical Modeling of Aqueous Systems II. American Chemical Society, Washington DC, pp. 212–225.
Stumm, W., Morgan, J.J. (Eds.), 2004. Aquatic Chemistry. Wiley, New York. 1024 pp.
van der Lee, J., 1998. Thermodynamic and mathematical concepts of CHESS. Technical report LHM/RD/98/3.
van der Lee, J., 2004. http://www.ctdp.org.
van der Lee, J., Lomenech, C., 2004. Towards a common thermodynamic database for speciation models. Radiochim. Acta 92, 811–818.
van der Lee, J., De Windt, L., Lagneau, V., Goblet, P., 2003. Module-oriented modeling of reactive transport with HYTEC. Comput. Geosci. 29, 265–275.
Velde, B. (Ed), 1995. Origin and Mineralogy of Clays. Clays and the Environment. Springer, Berlin Heidelberg New York, 334 pp.